crystals

MDPI

Article

Evolution of the Structural and Phase Composition of Ni–Ti–Cu Alloy Produced via Spark Plasma Sintering After Aging

Danagul Aubakirova [1], Elfira Sagymbekova [1], Yernat Kozhakhmetov [1], Yerkhat Dauletkhanov [1], Azamat Urkunbay [1], Dias Yerbolat [1], Piotr Kowalewski [2] and Yerkezhan Tabiyeva [1,*]

[1] Center of Excellence "VERITAS", D. Serikbayev East Kazakhstan Technical University, Ust-Kamenogorsk 070004, Kazakhstan; daubakirova@edu.ektu.kz (D.A.); esagymbekova@edu.ektu.kz (E.S.); ykozhakhmetov@ektu.kz (Y.K.); edauletkhanov@edu.ektu.kz (Y.D.); aurkunbay@edu.ektu.kz (A.U.); dyerbolat@edu.ektu.kz (D.Y.)

[2] Faculty of Mechanical Engineering, Department of Fundamentals of Machine Design and Mechatronic Systems, Wroclaw University of Science and Technology, 50-370 Wroclaw, Poland; piotr.kowalewski@pwr.edu.pl

* Correspondence: etabieva@edu.ektu.kz

Abstract

This study investigates the control of the phase-structural state in Ni–45Ti–xCu (x = 5, 7 at.%) shape memory alloys fabricated via a shortened powder metallurgy route: mechanical activation → spark plasma sintering (SPS) → heat treatment. Compact samples were produced from mechanically alloyed powders (650–750 rpm, up to 5 h) and sintered at 900 °C. The structure and microstructure were characterized using X-ray diffraction (to identify B2/B19′/Ni_4Ti_3 phases and assess ordering) and SEM–BSE/EDS (to analyze morphology, porosity, and Ni-rich precipitates). Two post-processing treatments were applied: single-stage annealing (500 °C, 2 h) and a three-stage treatment (900 °C/30 min → water quenching → 300 °C/20 min). Mechanical alloying transformed the initial elemental powder mixture (fcc-Ni, hcp-Ti, fcc-Cu) into a supersaturated fcc-(Ni, Cu, Ti) solid solution with emerging NiTi phases, with a minimum particle size achieved after ~300 min at 750 rpm. SPS compaction yielded a high-density matrix consisting predominantly of the B2 phase. Single-stage annealing preserved B19′ martensite and Ni_4Ti_3 precipitates, particularly in the 5 at.% Cu alloy. In contrast, the three-stage treatment dissolved the Ni_4Ti_3 precipitates, suppressed the formation of B19′ and R phases, and stabilized a highly ordered B2 matrix. Increasing the Cu content from 5 to 7 at.% significantly enhanced the B2 phase fraction, reduced secondary nickel-rich phases, and improved structural homogeneity, evidenced by a continuous neck network and closed porosity. The optimized condition—7 at.% Cu combined with the three-stage annealing—produced a microstructure with >95% B2 phase, <1% Ni_4Ti_3, and ~98% relative density. This forms the prerequisite microstructural state for a narrow transformation hysteresis and high functional cyclic stability.

Keywords: spark plasma sintering (SPS); aging treatment; thermal hysteresis; shape memory; Ni–Ti–Cu; mechanosynthesis; sintering; phase composition; microstructure; powder metallurgy

check for updates

Academic Editor: Alla S. Sologubenko

Received: 30 September 2025
Revised: 22 October 2025
Accepted: 29 October 2025
Published: 30 October 2025

Citation: Aubakirova, D.; Sagymbekova, E.; Kozhakhmetov, Y.; Dauletkhanov, Y.; Urkunbay, A.; Yerbolat, D.; Kowalewski, P.; Tabiyeva, Y. Evolution of the Structural and Phase Composition of Ni–Ti–Cu Alloy Produced via Spark Plasma Sintering After Aging. *Crystals* **2025**, *15*, 939. https://doi.org/10.3390/cryst15110939

Copyright: © 2025 by the authors. Licensee MDPI, Basel, Switzerland. This article is an open access article distributed under the terms and conditions of the Creative Commons Attribution (CC BY) license (https://creativecommons.org/licenses/by/4.0/).

1. Introduction

Binary Ti–Ni shape memory alloys (SMAs) exhibit unique functional properties—shape memory effect (SME) and superelasticity (SE)—due to the reversible thermoelastic

martensitic transformation between the high-temperature B2 austenite phase and the low-temperature B19′ martensite phase [1,2]. Consequently, these alloys are now widely used in industrial and biomedical engineering [3–5]. These materials are critical for hydraulic tube couplings, antenna assemblies, temperature-control systems, sensors, and actuators in the aerospace [6,7] and automotive industries [8,9], as well as in robotics [10,11]. In medicine, they are employed as materials for palatal arches, intraspinal implants, venous filters, eyeglass frames, microwires, stent grafts, intramedullary rods, and more in cardiovascular, neurosurgical, orthodontic, and orthopedic applications [12,13]. Additionally, Ti–Ni is being actively introduced in microsystem technology (sensors and micro devices) [14,15].

Despite the maturity of the field, the practical implementation of Ti–Ni-based SMAs is limited by two interrelated issues: functional fatigue and relatively low or unstable phase transformation temperatures. Under cyclic thermal loading, the SME and SE characteristics degrade—a phenomenon known as functional fatigue [16]. Typically, the characteristic transformation temperatures decrease with an increasing number of cycles due to the accumulation of dislocations, which disrupts the crystallographic compatibility between austenite and martensite [17]; this fatigue also deteriorates superelastic behavior. As a result, the reliability of Ti–Ni alloys remains insufficient for applications requiring high durability and precise control, such as elastocaloric cooling and artificial heart valves. Efforts to mitigate this problem focus on tailoring composition and microstructure. For instance, alloying with Cu (e.g., in $Ti_{54}Ni_{34}Cu_{12}$ thin films) enhances transformation stability under thermal cycling and maintains nearly unchanged superelasticity up to ~10^7 cycles [18].

Various technologies are used to produce Ni–Ti–Cu, among which conventional casting remains the industrial standard [13,14,19,20]. However, this multi-stage melting–casting–post-processing route does not guarantee complete chemical homogeneity of the ingot. It can lead to micro- and macrosegregation, oxidation, increased impurity levels, and is characterized by high energy consumption (especially for systems with refractory components) as well as a need for specialized equipment [21,22]. These limitations have stimulated the search for more direct and cleaner synthesis routes for obtaining semi-finished products and components [23,24].

A promising alternative is powder metallurgy (PM), which allows for the formation of parts at temperatures below the melting points of the components, thereby minimizing oxygen and carbon contamination. Ni-Ti parts produced using PM methods typically exhibit a finer, more uniform microstructure and improved processing properties.

Among modern PM methods, spark plasma sintering (SPS) stands out. This technique consolidates powder in a graphite die under uniaxial pressure and a pulsed direct current. The combined action of electrothermal heating and pressure accelerates mass transfer, ensures rapid heating, and limits grain growth; for refractory powders, a relative density of ~99% is achievable [25–27]. For SMAs, the SPS process is implemented at relatively low temperatures (approximately 900–1100 °C) and short holding times, which promotes uniform sintering and reduces the likelihood of undesirable reactions. According to [28], SPS enables the production of compounds of almost any composition. Its advantages over traditional technologies include low sintering temperatures, short processing times (on the order of minutes), low energy consumption (approximately one-fifth that of hot pressing), uniform heating, controllable temperature gradients, no need for additives or plasticizers, the ability to sinter powders with a wide particle size distribution, high final density, single-step processing, and surface cleaning of particles under the influence of the electric current.

Despite these advantages, the literature on Ni–Ti–Cu alloys produced via SPS is significantly less extensive than for alloys produced via melting. Meanwhile, Ni–Ti–Cu systems are promising in terms of the stability of their functional properties (demonstrating

stability up to 10^7 thermal cycles for certain compositions [18]). However, their functional characteristics after SPS have only been studied fragmentarily, without a detailed analysis of the "structural-phase state ↔ functional response" relationship.

The addition of Cu to Ti–Ni–Cu shape memory alloys is a well-established approach to controlling transformation characteristics. Partial substitution of Ni by Cu stabilizes the B2 austenite phase, promotes a single-step B2→B19 transformation, and reduces thermal hysteresis by improving lattice compatibility at the austenite/martensite interface. Within the low-Cu range, increasing Cu content gradually lowers and narrows the M_s/Af temperature interval toward room temperature while preserving reversibility. However, excessive Cu (>10–12 at.%) promotes embrittlement and secondary phase formation, reducing functional durability [29]. Therefore, compositions with 5–7 at.% Cu are considered optimal for achieving near-room-temperature transformation behavior with good ductility and stability. In this work, $Ni_{45}Ti_xCu_x$ alloys with x = 5 and 7 at.% were selected to represent this composition range and to assess the influence of Cu content on phase stability, microstructure, and transformation behavior under identical SPS processing conditions.

The aim of this work is to obtain compact Ni–Ti–Cu samples using the SPS method and to establish the relationship between the SPS parameters, heat treatment, microstructure, and phase composition.

2. Materials and Methods

The objects of the study were samples from a system of shape memory alloys:

1. Ni–45Ti–5Cu (at.%).
2. Ni–45Ti–7Cu (at.%).

The Cu content of 5–7 at.% was selected to ensure a single-stage B2→B19 transformation and a narrower thermal hysteresis compared to binary NiTi, while avoiding the embrittlement region that occurs at Cu concentrations above ~12.5 at.% in Ti–Ni–Cu alloys [29]. This composition range also enables the tuning of Ms and Af temperatures near room temperature following U-FAST/SPS processing. The specific pair of compositions—$Ni_{45}Ti_{50}Cu_5$ and $Ni_{45}Ti_{48}Cu_7$—provides a sensitive comparison of the effect of Cu content at a near-constant base stoichiometry, which is ideal for analyzing the "SPS parameters → microstructure → functional response" relationship [30,31].

The alloys were produced by combining mechanosynthesis and Spark Plasma Sintering from a three-component Ni–Ti–Cu powder mixture (parameters and scheme are given in Table 1 and Figure 1). The following powders with an average particle size of 10–50 μm, weighed according to the nominal Ni–Ti–Cu composition, were used as starting materials for obtaining the shape memory alloys: nickel powder (Si ≤ 0.003; Fe ≤ 0.001; Zr ≤ 0.002; Cu ≤ 0.001; C ≤ 0.002); titanium powder (Fe ≤ 0.002; Cr ≤ 0.003; Ni ≤ 0.002; Cu ≤ 0.003; Ta ≤ 0.002); and copper powder (main impurities: Al ≤ 0.002; Fe ≤ 0.001; Cr ≤ 0.001; Ni ≤ 0.001; Si ≤ 0.002) with 99% purity, supplied by Hebei Suoyi New Material Technology, Handan, China.

Mechanosynthesis was performed using a Pulverisette 7 Premium Line planetary mill (Fritsch GmbH, Idar-Oberstein, Germany). To mitigate agglomeration and ensure uniform dispersion of the metallic components, stearic acid was used as a Process Control Agent (PCA), with its concentration adjusted from 2.5 wt.% to 3.0 wt.% for longer milling durations. Extensive preliminary milling series (up to 8 hours) confirmed that abrasive wear of the milling media had no significant impact on the final chemical composition. This is attributed to the use of an optimal ball-to-powder mass ratio (10:1), which reduces specific load on the surfaces, and the controlled argon atmosphere, which prevents oxidation and reactions with wear products.

Table 1. Detailed parameters for obtaining a three-component shape memory alloy.

Mixing/Mechanosynthesis				
Mill rotation speed	Materials used for balls and container	Ratio of milling balls to powder mixture	Process duration, minutes	Chemical agents
650 rpm/750 rpm	Stainless steel/ball size 5 mm/cup volume 45 mL	10:1	60/180/300/480	-/Stearic acid
Spark Plasma Sintering				
Pressure	Heating speed	Holding time, minutes	Maximum temperature	Environment
49.2 MPa	100 °C/min	10 min	900 °C	Vacuum

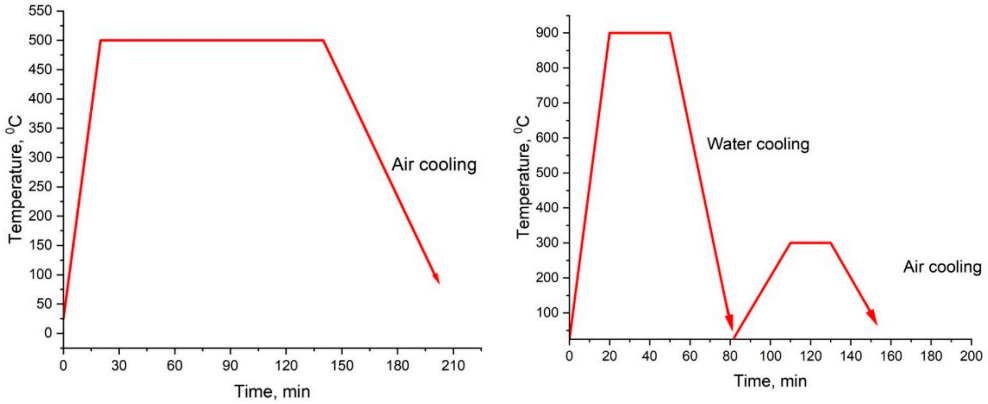


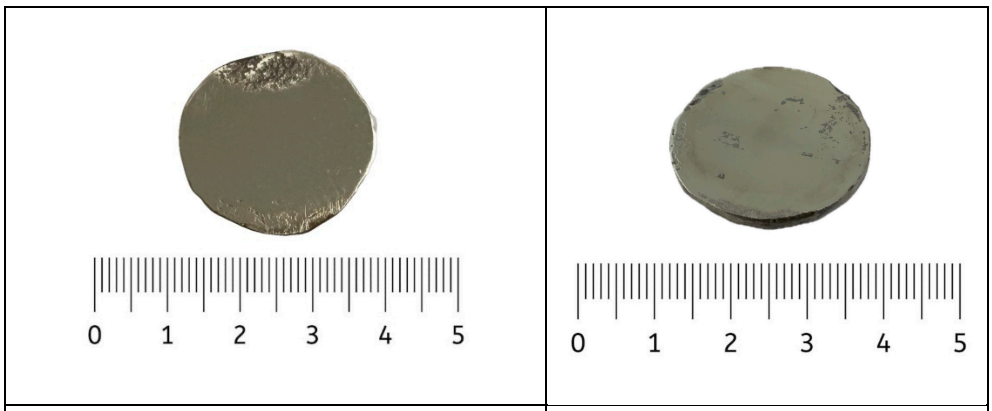
Figure 1. Appearance of Ni–Ti–Cu alloy samples after SPS: (**a**) Ni–45Ti–5Cu (at.%); (**b**) Ni–45Ti–7Cu (at.%).

In addition, stearic acid was introduced into the powder mixture as a process control agent (PCA) in the amount of 2.5 wt.% and 3 wt.% relative to the total mass of the solid phase. The increase in PCA concentration with longer milling duration was aimed at counteracting the higher risk of particle agglomeration and ensuring continuous dispersion of metallic components within the matrix.

Based on the analysis of the phase composition and morphology of the mechanosynthesized powders, optimal SPS parameters were selected from literature [1–3,18–23] and preliminary experiments. The goal was to achieve effective densification while preserving the B2 and B19′ phases responsible for the shape memory effect and minimizing undesirable phase transformations.

The consolidation of the powder mixtures was carried out on a GeniCore U-FAST GC unit (GeniCore, Warsaw, Poland) under vacuum using a pulsed direct current. The U-FAST GC system provides programmable control of heating rate, uniaxial stress, current/pulse parameters, and holding time. The compacts were formed in a fine-grained graphite die (inner diameter 20 mm), and a 0.1 mm thick graphite foil was used to prevent the powders from sticking to the die during pressing.

The choice of the specified temperature–pressure window was based on data for NiTi/Ni–Ti–Cu: an achievable relative density of ≈98% already at ~900 °C (for fine particles) and a strong dependence of densification/microstructure on temperature, particle size, and applied load. Figure 2 shows the appearance of the compacts after sintering.



Ni–45Ti–5Cu (at.%)	Ni–45Ti–7Cu (at.%)
(**a**)	(**b**)

Figure 2. Annealing schedule for Ni–Ti–Cu alloy samples: (**a**) Single-stage annealing; (**b**) three-stage annealing.

After Spark Plasma Sintering, four square samples measuring 5 × 5 × 2 mm were cut from the Ni–Ti–Cu alloy compacts for subsequent heat treatment (Table 2).

Table 2. Annealing parameters of Ni–Ti–Cu.

№	Temperature	Time	Cooling
1	500 °C	2 h	in the air
2	900 °C	30 min	rapid hardening (water)
	300 °C	20 min	in the air

Samples in the first group were subjected to a single-stage annealing process: heating at 25 °C/min to 500 °C, holding for 2 h, and then cooling to room temperature. This process stabilizes the phase composition and promotes the precipitation of dispersed particles, which affect the martensitic transformation temperatures and mechanical properties of shape-memory alloys.

The second group of samples was treated using a three-step scheme aimed at eliminating the intermetallic Ni_4Ti_3 phase and stabilizing the solid solution without its reformation. In the first step, solution annealing was carried out at 900 °C for 30 min in an SNOL 30/1100 furnace at a heating rate of 45 °C/min, ensuring effective dissolution of the Ni_4Ti_3 phase and homogenization of the matrix. After annealing, the samples were rapidly quenched in water to suppress re-precipitation of Ni_4Ti_3. In the final step, a low-temperature annealing at 300 °C for 20 min was performed in an SNOL 6.7/1300 furnace at a heating rate of 15 °C/min, followed by cooling to room temperature. This regime helps relieve residual internal stresses without causing precipitation of the Ni_4Ti_3 phase, which typically occurs within the temperature range of 350–500 °C.

After each treatment stage, the samples were prepared for analysis using a Struers grinding and polishing system with water cooling. Surface preparation involved sequential grinding with silicon carbide abrasive papers of P400, P600, P800, and P1200 grit sizes, followed by polishing on a cloth using diamond suspensions with particle sizes of 3 μm and 1 μm. To reveal the microstructure, the polished samples were chemically etched in a solution consisting of concentrated nitric acid (HNO_3, 65–68 wt.%) and hydrochloric acid (HCl, 32–35 wt.%) mixed in a 1:3 volume ratio (corresponding to approximately a 1:2 mass ratio of pure components). The samples were then analyzed to evaluate the

phase composition, microstructure, and morphological changes occurring during the compaction process.

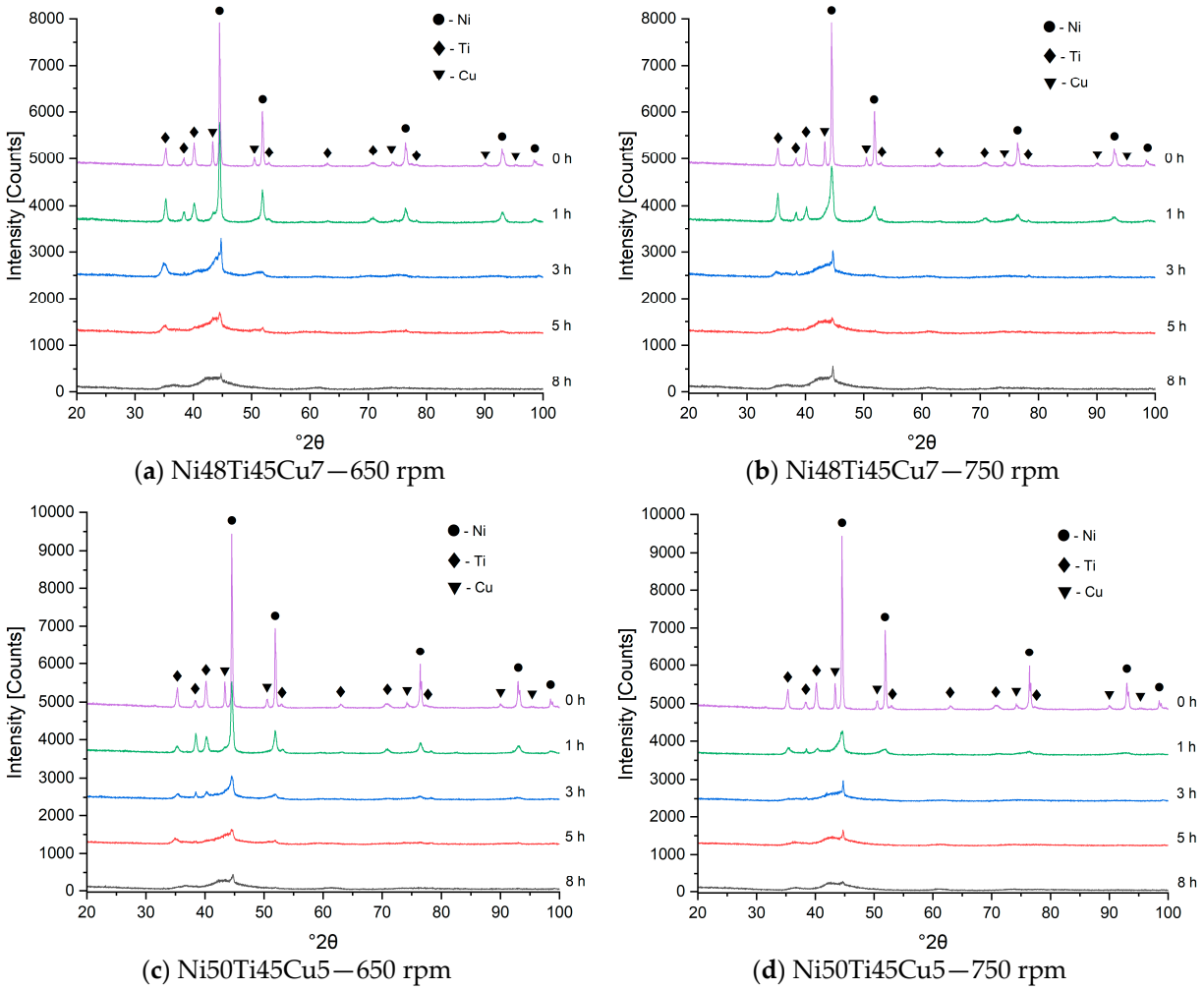
The crystalline characteristics and phase composition of the alloy samples were examined using an X'Pert PRO X-ray diffractometer (Malvern Panalytical Empyrean, Almelo, The Netherlands) with a copper anode. Diffraction patterns were recorded in the 2θ range of 20–100°, at a tube voltage of 45 kV and a tube current of 40 mA. The scanning step was 0.02°, with a counting time of 1.5 s per step. Diffraction data were processed and analyzed using Highscore software (Version 4.9a) processing and search software.

Morphological evolution was studied using a scanning electron microscope (Phenom ProX, Thermo Fisher Scientific, Waltham, MA, USA), and particle size distribution was studied using a laser diffraction analyzer (Analysette 22 NeXT Nano, Fritsch, Germany).

3. Results and Discussion

3.1. Phase Composition of Powder Mixtures After Mechanical Activation

According to the results of phase analysis, powders of both compositions have a similar evolution pattern; the difference is observed only in the intensity of individual peaks (see Figure 3).



(**a**) Ni48Ti45Cu7—650 rpm (**b**) Ni48Ti45Cu7—750 rpm

(**c**) Ni50Ti45Cu5—650 rpm (**d**) Ni50Ti45Cu5—750 rpm

Figure 3. X-ray diffraction patterns of alloys after high-energy processing in a planetary mill.

The diffraction patterns of the initial powder mixtures exhibit sharp, intense peaks corresponding to the metallic phases fcc-Ni (a ≈ 3.519 Å), hcp-Ti (a ≈ 2.950 Å, c ≈ 4.686 Å), and fcc-Cu (a ≈ 3.610 Å), indicating a high degree of crystallinity of the starting components.

After ~1 h of high-energy milling, the peaks of all components start to weaken and broaden, reflecting a reduction in the average crystallite size and an increase in microstrain caused by intensive plastic deformation during particle collisions. At 750 rpm, all Cu reflections and most Ti peaks disappear in all compositions examined; at 650 rpm, a similar disappearance of Cu is observed, with only a weak (111) Cu reflection remaining, while several Ti peaks are still partially present.

The vanishing of Cu reflections and the systematic shift of Ni peaks to lower 2θ angles (increase in lattice parameter) indicate the dissolution of Cu in the Ni lattice and partial dissolution of Ti, leading to the formation of a supersaturated fcc-(Ni, Cu, Ti) solid solution. This is facilitated by the close atomic radii of Cu (≈1.28 Å) and Ni (≈1.24 Å) and the significantly larger radius of Ti (≈1.47 Å), making Cu highly soluble and Ti only partially soluble in fcc-Ni.

After ~3 h of mechanical activation at 650 rpm, the fcc-Ni and hcp-Ti reflections are still identified but strongly broadened; at 750 rpm, they transform into a diffuse halo, indicating progressive amorphization. This behavior occurs due to the accumulation of crystal defects—dislocations, stacking faults, and subgrain boundaries—which reduce diffusion distances and accelerate interdiffusion even under localized moderate heating.

After ~5 h of treatment at 650 rpm, weak peaks of NiTi intermetallics—high-temperature cubic B2 and martensitic monoclinic B19′—appear against the amorphous background. At 750 rpm, the formation of these peaks occurs earlier and more distinctly, as expected from the higher specific impact energy. By ~8 h, the intensities of the B2 and B19′ reflections increase in all compositions, indicating a growth in their volume fraction.

The effect of Cu becomes increasingly pronounced at the NiTi nucleation stage: the composition with 7 at.% Cu demonstrates earlier and more intense formation of B2/B19′ phases compared to 5 at.% Cu. This is consistent with the role of Cu in promoting interdiffusion and atomic ordering in the Ni–Ti–Cu system. The peak broadening throughout milling is attributed to the combined influence of coherent domain refinement and increasing lattice microstrain. The continuous shift of Ni peaks to lower 2θ values confirms lattice expansion due to the substitution of Ni atoms by larger Cu and partially by Ti.

Summary of the evolution during mechanical activation (5–7 at.% Cu).

Initial state: crystalline fcc-Ni, hcp-Ti, fcc-Cu.

1–3 h mechanical activation: dissolution of Cu in Ni, partial dissolution of Ti; formation of supersaturated fcc-(Ni, Cu, Ti); increase in microstrain; onset of amorphization (especially at 750 rpm).

~5 h mechanical activation: weak NiTi (B2/B19′) reflections appear on the amorphous background; at 750 rpm, they appear earlier and more pronounced.

~8 h mechanical activation: an increase in the B2/B19′ proportion in all compositions; at 7 at.% Cu, the phase formation rate is higher compared to 5 at.% Cu.

Thus, high-energy mechanical activation sequentially transforms the system from the initial metallic phases to a supersaturated fcc solid solution, then to a partially amorphous state, and finally to the nucleation and growth of NiTi intermetallics (B2/B19′). Furthermore, raising the Cu content from 5 to 7 atomic percent significantly speeds up all stages related to the formation of NiTi.

3.2. Morphology and Phase State of Ni–45Ti–7Cu and Ni–45Ti–5Cu (at.%) Powders After Mechanical Alloying

Figure 4 presents SEM micrographs of the powders after mechanical activation at different milling conditions. Following preliminary mixing (2 h), a simple mechanical mixture of Ni, Ti, and Cu particles is observed, without noticeable fragmentation or interdiffusion;

particle contact remains superficial and insufficient to initiate reaction or cold welding in the absence of high-impact energies [32–34].

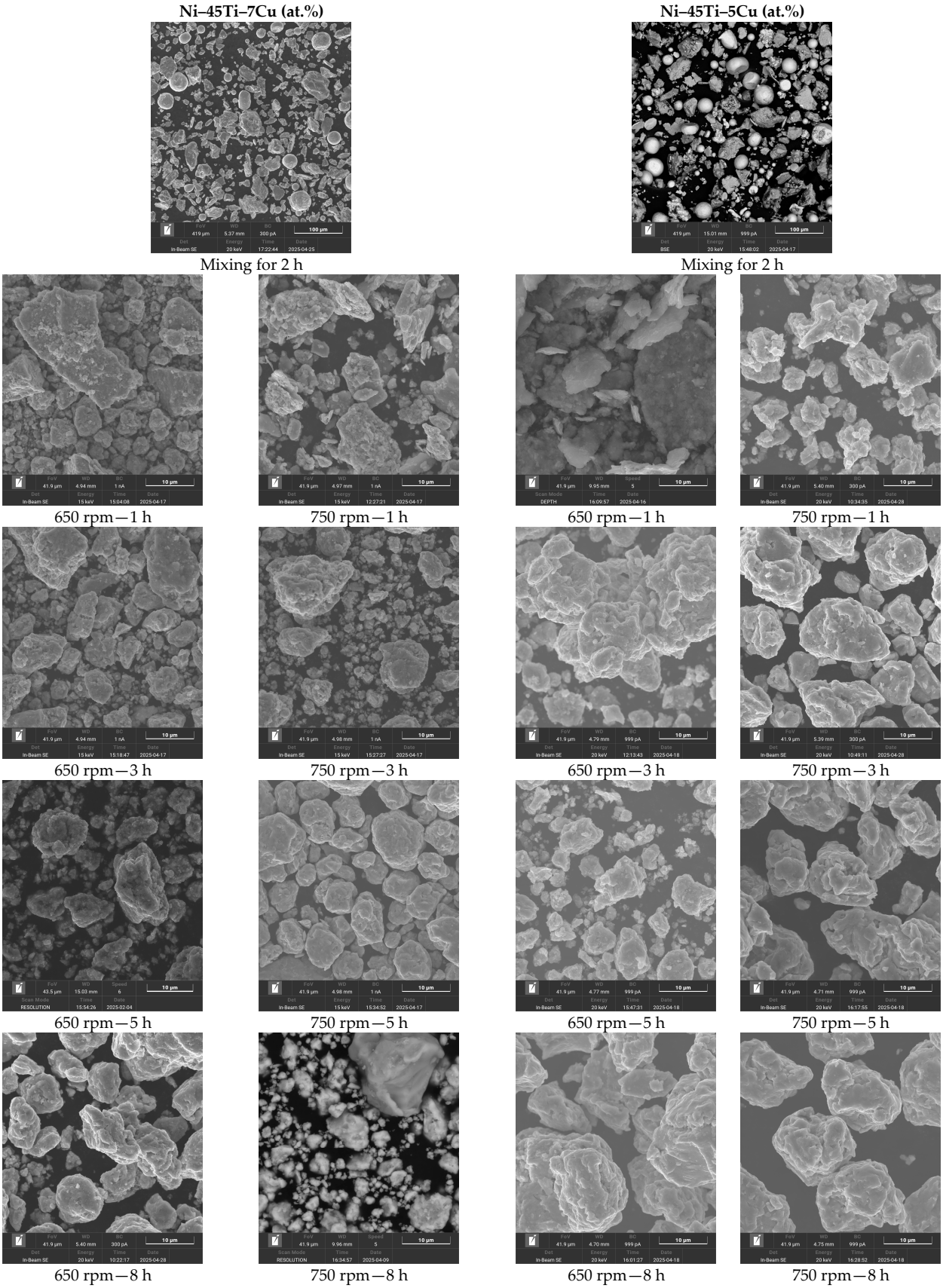


Figure 4. Evolution of powder particle morphology during mechanochemical activation.

Transitioning to MA regimes (650–750 rpm) initiates the typical "cold welding ⇄ fracturing" cycle, resulting in the formation of a lamellar or flake-like morphology and the appearance of neck-shaped bridges between compacted layers. Increasing the milling speed from 650 to 750 rpm significantly raises the collision energy, enhances defect accumulation (dislocations, stacking faults, subgrains), and shortens diffusion pathways. Consequently, particles become thinner, agglomerates more consolidated, and partial amorphization is increasingly detected in the powder mass [35–37].

The 7 at.% Cu composition demonstrates more intensive and earlier plastic agglomeration compared to 5 at.% Cu, which is attributed to Cu acting as a softer phase—similar in size to Ni—and dissolving more readily into the Ni lattice. In XRD, this is reflected in the faster disappearance of Cu peaks (especially at 750 rpm) and a more pronounced shift of Ni reflections to lower 2θ values, confirming lattice expansion and the formation of a supersaturated fcc-(Ni, Cu, Ti) solid solution characterized by limited Ti solubility [35–37].

With increasing milling time (1–8 h), the broadening of diffraction peaks becomes more distinct due to reduced coherent domain size and rising microstrain, while weak reflections of NiTi intermetallics (B2 and B19′) appear and intensify with time. These indicators of reaction-diffusion phase nucleation are more evident at 750 rpm and/or at 7 at.% Cu. At 650 rpm and 5 at.% Cu, longer treatment is required to reach a comparable state. The resulting morphology—thin lamellae with necks and dense agglomerates featuring high defect density—is consistent with published observations for NiTi(–Cu) powders, where increasing milling energy accelerates the transition from crystalline metallic phases to a partially amorphous matrix containing newly formed NiTi phases [36–38].

Moreover, in Cu-containing NiTi powders, the martensitic transformation has been shown to shift toward a single-step B2 → B19 transition with considerably reduced hysteresis compared to binary NiTi (where B2 → B19′ dominates) [30,38]. Transformation temperatures depend strongly on Cu content. For gas-atomized Ti–Ni–Cu powders containing 5, 10, and 20 at.% Cu, reported Ms values are approximately −4.9, −17.6, and +32.1 °C, respectively, while (Af–Ms) decreases markedly with growing Cu content (from ~20 down to ~7 °C). These trends provide solid expectations for our compositions with 5–7 at.% Cu: a narrower hysteresis loop and earlier "maturation" of B2/B19 phases under comparable processing conditions [30,39,40].

For subsequent SPS/U-FAST consolidation, such a lamellar, sheet-like, necked, and defect-enriched structure is advantageous: it reduces diffusion distances and lowers the energy threshold of reactions, thereby facilitating the attainment of high density at moderate sintering temperatures and promoting the formation of a "clean" functional response characteristic of one-step B2 → B19 kinetics. It is expected that Ni–45Ti–7Cu powders will exhibit a narrower hysteresis loop and better cyclic stability of functional properties compared to Ni–45Ti–5Cu, fully consistent with the trends reported for Ti–Ni–Cu powders and bulk materials in the literature.

Figure 5 shows SEM images of the same powder region at magnifications of ×5000 (scale bar 10 μm) and ×33,000 (scale bar 2 μm). At lower magnification ×5000, a polydisperse mixture of particles with pronounced bimodality is clearly visible: along with coarse cores (on the order of several microns), a large number of submicron-scale satellites are present, adhered to their surfaces. Interparticle necks and smoothed edges indicate cycles of cold welding and crushing, characteristic of mechanical alloying. This "core-satellite" morphology corresponds to a stage of intense surface activation and shortening of diffusion paths.

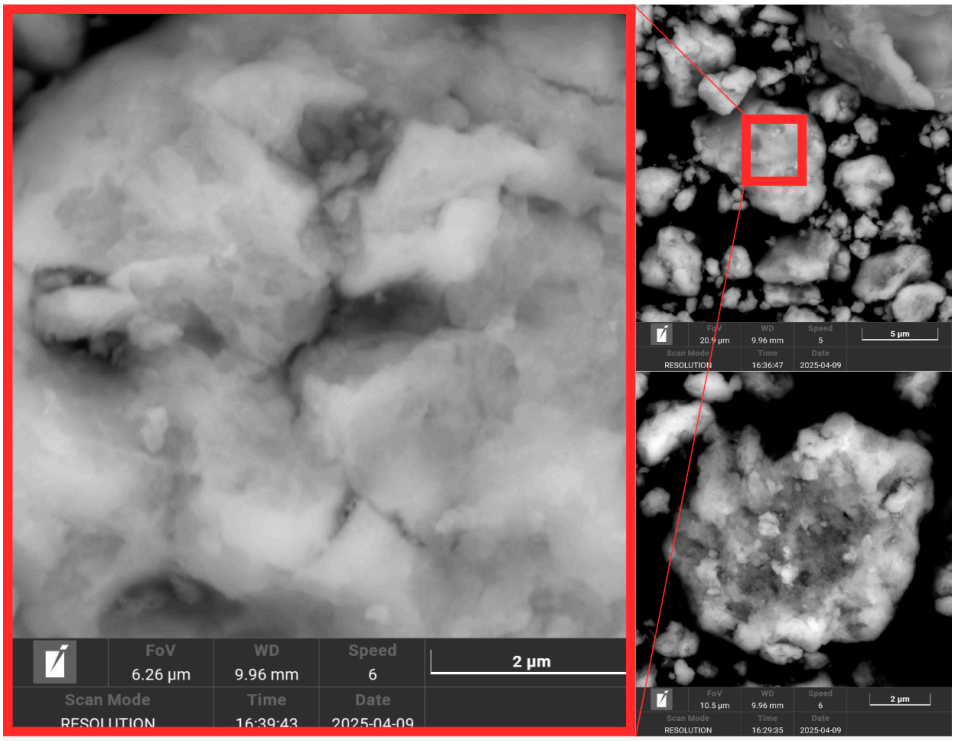


Figure 5. Surface morphology of Ni–45Ti–7Cu (at.%) powder particles after 8 h at 750 rpm.

At higher magnification (×33,000), the surface of a large particle exhibits a coarse-grained, "cauliflower-like" relief formed by aggregates on the nanometer–submicron scale (approximately 0.1–0.3 µm), with a system of shallow grooves and shear steps. The presence of numerous necks between nano-aggregates and micropores confirms intense plastic deformation and multicycle rewelding, leading to nanocrystallization/partial amorphization of the surface layer.

The results (see Table 3) of the powder particle analysis reveal three key findings.

Table 3. Particle analysis.

	Ni–45Ti–5Cu (at.%).		Ni–45Ti–7Cu (at.%).	
Milling Time, min	**Particle Sizes (650 rpm), µm**	**Particle Sizes (750 rpm), µm**	**Particle Sizes (650 rpm), µm**	**Particle Sizes (750 rpm), µm**
initial	54.51 ± 0.2			
60	15.47 ± 0.11	15.95 ± 0.04	12.815 ± 0.05	10.129 ± 0.09
180	12.524 ± 0.1	10.5 ± 0.05	9.68 ± 0.02	10.96 ± 0.02
300	10.37 ± 0.06	8.32 ± 0.05	8.52 ± 0.01	7.97 ± 0.02
480	26.36 ± 0.06	21.27 ± 0.004	20.79 ± 0.05	16.329 ± 0.006

First, during the early stages of milling, 7 at.% Cu accelerates the refinement of particles, resulting in smaller sizes by the 60th minute; this is consistent with the higher plasticity of the Ni–Cu-rich matrix and enhanced interdiffusion.

Second, the minimum average particle size is reached at around 300 min under all conditions; among these, 750 rpm produces the finest dispersion (7.97–8.32 µm).

Third, during prolonged milling (480 min), particle coarsening begins due to cold welding; however, this effect can be significantly mitigated by combining a higher rotation speed (750 rpm) with a higher Cu content (7 at.%).

After 8 h of mechanical activation, the average particle size increased noticeably, with large welded agglomerates reaching 20–27 µm compared to 8–10 µm after 3–5 h of milling.

This growth is attributed to a shift from fracture-dominated refinement to cold welding and particle coalescence during prolonged milling, as highly deformed ductile surfaces tend to adhere upon repeated impacts. Such a transition from fragmentation to agglomeration has been widely reported in mechanically alloyed systems [37,38], including NiTi and NiTiCu alloys, where extended milling promotes the formation of welded clusters and changes in particle morphology. These observations are consistent with results and confirm that the increase in agglomerate size is a natural consequence of cold welding during long-term mechanical alloying.

From a practical standpoint, the optimal mode for minimizing particle size and suppressing subsequent coarsening is approximately 5 h at 750 rpm; if the priority is the fastest size reduction at early stages, the Ni–45Ti–7Cu composition also shows an advantage. The measurement errors are small (±0.004–0.11 μm), making the observed differences statistically reliable at a descriptive-comparative level. Consequently, for subsequent sintering work, samples milled for 5 h at 750 rpm were selected.

3.3. Microstructure and Phase Composition of Composites of Ni–Ti–Cu Powder Mixtures

Figure 6 presents the X-ray diffraction patterns of the compact samples obtained by spark plasma sintering (SPS) at 900 °C from powders of Ni–45Ti–5Cu and Ni–45Ti–7Cu compositions (at.%), hereafter referred to as "5% Cu" and "7% Cu." In both materials, the phases of the NiTi system are clearly identified: austenitic B2, martensitic B19′, and the Ni-rich intermetallic Ni_4Ti_3. The sharp and intense reflections indicate a high degree of ordering and recrystallization during SPS, consistent with the well-known enhancement of diffusion, localized Joule heating at particle contacts, and rapid neck formation under simultaneous pulsed current and applied pressure. As a result, sintering at 900 °C leads to the formation of a highly dense structure with predominant B2 austenite and a reduced fraction of secondary phases [32].

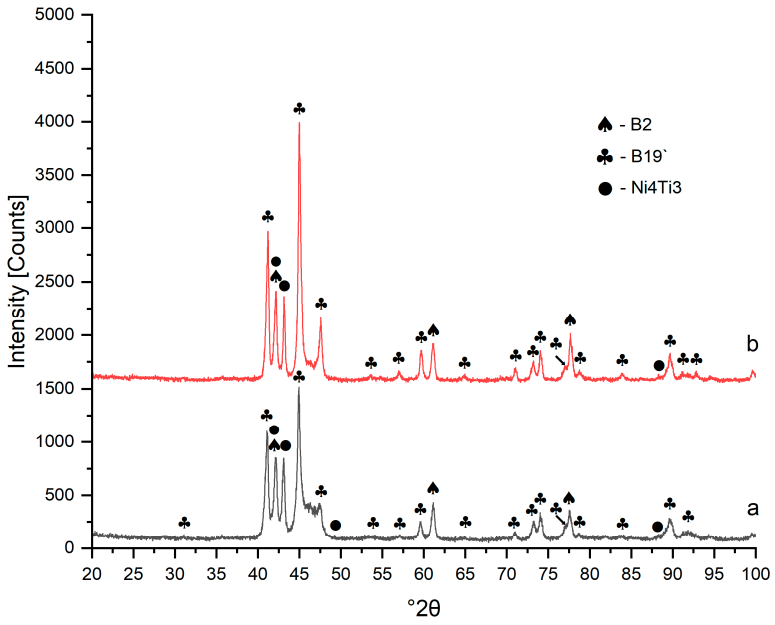


Figure 6. X-ray diffraction patterns of Ni–Ti–Cu system alloys after SPS: (**a**) Ni–45Ti–5Cu 750 rpm at 900 °C; (**b**) Ni–45Ti–7Cu 750 rpm at 900 °C.

A comparison of the diffraction patterns reveals that in the 7% Cu sample, the relative intensity of B2 reflections is higher, whereas the B19′ and Ni_4Ti_3 peaks are noticeably suppressed compared with the 5% Cu sample. This trend aligns with the established role of copper as a stabilizer of the single-step B2 → B19 transformation in Ti–Ni–Cu alloys and its

ability to reduce thermal hysteresis, in contrast to binary NiTi, which typically undergoes the B2 → B19′ transition with a wider hysteresis loop. Thus, Cu addition enhances chemical and phase homogeneity, promotes B2 formation, and reduces the precipitation of Ni-rich particles such as Ni_4Ti_3 [30].

The presence of Ni_4Ti_3 in both samples is attributed to SPS processing kinetics: rapid heating and cooling, combined with transient nickel enrichment at interparticle interfaces, promote precipitation of Ni-rich intermetallics. However, with a higher Cu content (7 at.%), improved diffusion-driven homogenization suppresses their accumulation, which is reflected in the lower intensities of the corresponding reflections. According to published data on SPS-fabricated NiTi(–Cu) alloys, increasing the sintering temperature enhances the austenitic matrix and minimizes secondary phases such as Ni_3Ti, Ti_2Ni, and Ni_4Ti_3 due to more complete diffusion [32]. The observed dominance of B2 at 900 °C is also fully consistent with earlier reports for SPS-processed NiTi/NiTiCu systems [38], where elevated temperatures and pulsed current markedly accelerate densification and recrystallization, enabling high density (up to ~98% under comparable conditions) while effectively "cleaning" the matrix of excess phases.

Residual B19′ peaks after SPS at 900 °C are expected and may be associated with local internal stresses (including areas with residual porosity) and with the retention of part of the defective substructure not fully relieved during the short dwell time. Similar observations (the presence of austenite at room temperature and the transition to martensite upon cooling) have been reported for compact NiTi specimens after SPS [31]. Additional increases in SPS temperature/time and/or a brief subsequent annealing generally further stabilize B2 and reduce the fraction of nickel-rich precipitates.

A semi-quantitative phase analysis was performed using the Rietveld refinement method (Table 4), based on which the volume fractions of each phase were determined (in Figure 6).

Table 4. Phase analysis using the Rietveld refinement method.

	B2, %	**B19′, %**	**Ni_4Ti_3, %**
5% Cu	29.7	42.6	27.7
7% Cu	34.4	40.9	24.6

The analysis revealed that both alloys comprise three primary phases: the high-temperature austenitic B2 phase, the martensitic B19′ phase, and the secondary Ni_4Ti_3 phase. In the alloy with 5 at.% Cu, the phase fractions were 29.7% B2, 42.6% B19′, and 27.7% Ni_4Ti_3. Increasing the Cu content to 7 at.% resulted in a higher proportion of the B2 phase (34.4%) and a reduction in both the B19′ (40.9%) and Ni_4Ti_3 (24.6%) phases. These results indicate that Cu addition stabilizes the B2 austenitic phase and suppresses the formation of Ni-rich secondary phases. This is consistent with the known role of Cu in enhancing phase homogeneity and reducing crystallographic incompatibility in Ni–Ti–Cu systems.

Scanning electron microscopy (SEM) micrographs of samples sintered by Spark Plasma Sintering (SPS) at 900 °C reveal significant microstructural differences between the Ni–45Ti–5Cu and Ni–45Ti–7Cu alloys (Figure 7). At low magnification, the 5 at.% Cu alloy exhibits heterogeneous particle clusters, an incomplete interparticle neck network, and pronounced residual porosity. In contrast, the 7 at.% Cu alloy displays a more uniform structure with a well-developed neck network and predominantly closed micropores, indicating a higher degree of densification.

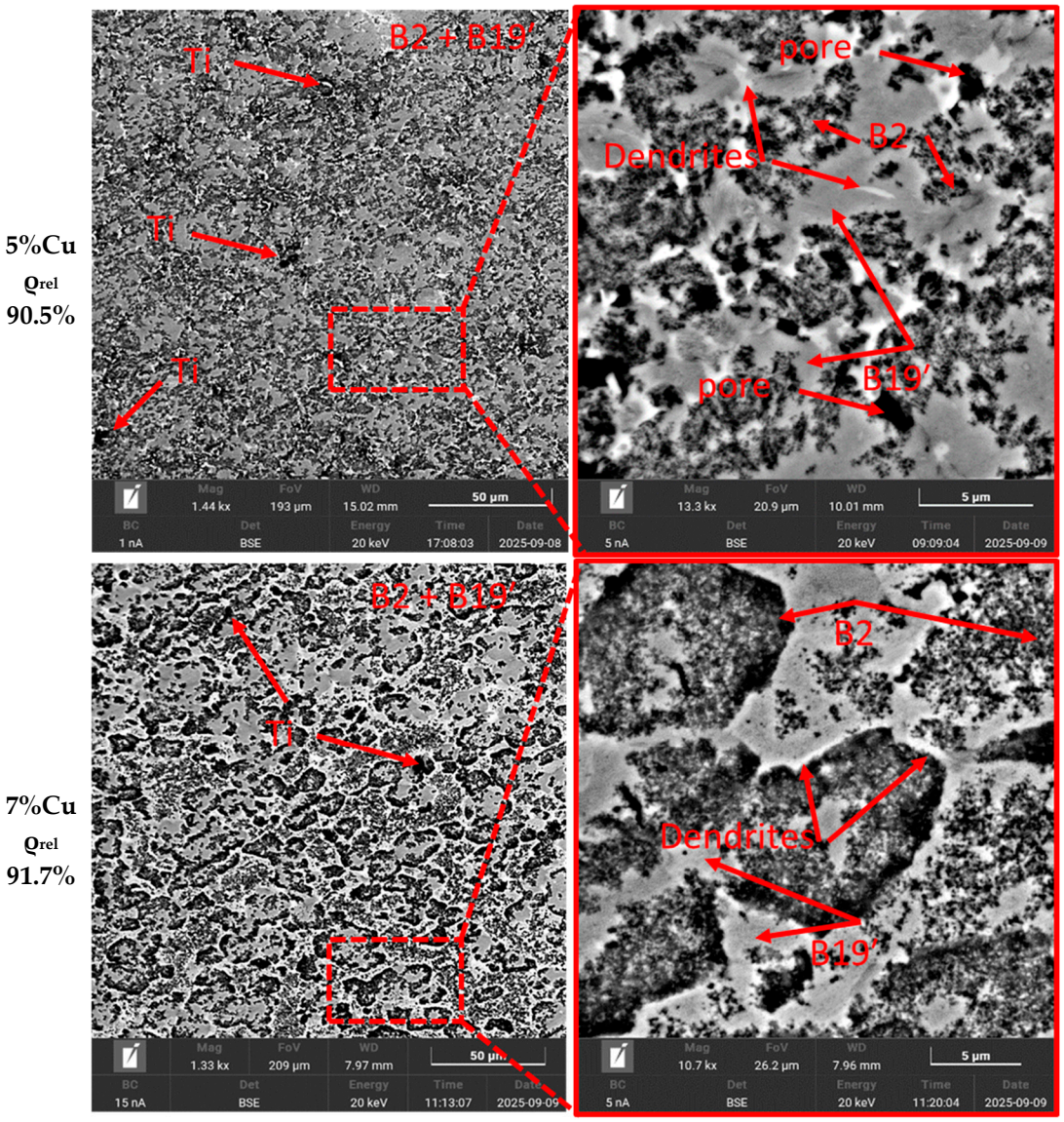


Figure 7. Surface of samples after SPS at 900 °C.

At higher magnification, the contrast is more evident. The 5 at.% Cu sample shows broken or narrow necks and a coarse matrix surface with scattered islands of small precipitates. Conversely, the 7 at.% Cu sample features continuous necks, a dense nanodispersed coating on the matrix surface, and isolated closed micropores. This microstructural evolution confirms that Cu increases the plasticity of the Ni-rich matrix and accelerates diffusion within the Ti–Ni–Cu system. This facilitates homogenization and the development of the B2 austenitic matrix during SPS, while reducing the tendency for Ni-rich precipitate accumulation (e.g., Ni_4Ti_3) and residual porosity. These trends align with published data on Ti–Ni–Cu powders and compacts, wherein Cu promotes a single-step B2 → B19 transformation with narrow thermal hysteresis compared to binary NiTi, and SPS enables high density and recrystallization at moderate temperatures [31,32,38].

Scanning Electron Microscopy (SEM) analysis reveals that increasing the copper content from 5 to 7 at.% significantly improves consolidation during spark plasma sintering (SPS) at 900 °C. At low magnification, the 5 at.% Cu compact exhibits heterogeneous particle clustering, an underdeveloped network of interparticle necks, and visible residual porosity. In contrast, the 7 at.% Cu compact displays a more uniform architecture with a well-connected neck network and predominantly closed micropores.

At higher magnification, the 5 at.% Cu sample shows a coarse matrix surface with narrow or locally fractured necks, along with scattered small precipitates. The 7 at.% Cu sample, however, features continuous necks and a dense nanodispersed surface layer, indicative of enhanced diffusion and plastic flow within the Ni–Cu-rich matrix. Consequently, the 7 at.% Cu alloy achieves higher effective density and microstructural homogeneity, providing a more favorable foundation for stabilizing the B2 austenite phase and suppressing Ni-rich secondary phases after SPS.

Isolated unreacted Ti particles are also observed on the surface, which appear as rounded pits or cavities, likely where particles were dislodged during mechanical polishing and chemical etching. This effect is more pronounced in the 5 at.% Cu alloy, consistent with its less complete diffusional homogenization and a lower Ni–Ti interdiffusion rate compared to the 7 at.% Cu variant.

Following single-stage annealing, the microstructure of the 5 at.% Cu sample remains heterogeneous (Figure 8a). It consists of recrystallized grains with blurred boundaries, chains of predominantly closed micropores, and localized particle clusters. The interparticle neck network is incomplete and locally interrupted, reflecting uneven densification after SPS and aging. On the matrix surface (Figure 8b), fine-dispersed bright precipitates—identified as Ni_4Ti_3 particles formed during aging at ~350–500 °C—are visible. Isolated dark depressions from dislodged Ti-enriched particles and locally narrow or broken necks are also present.

In contrast, the microstructure of the 5 at.% Cu sample after three-stage annealing is markedly more uniform (Figure 8c). It exhibits a coherent grain architecture with a well-defined necking network. Closed micropores predominate, alongside clear signs of homogenization and increased density. The number of bright Ni-rich precipitates is sharply reduced (Figure 8d). The matrix relief is smoothed, with continuous necks and only sparse traces of spalling.

After single-stage annealing, the microstructure of the samples containing 7 at.% Cu is significantly more homogeneous than that of the 5 at.% Cu alloy (Figure 9a). A well-developed, continuous network of interparticle necks is observed, with predominantly closed micropores and rounded, clearly defined grains. Small bright particles corresponding to Ni-rich precipitates are sparsely distributed within a smooth B2 matrix (Figure 9b). The surface relief is uniform, signs of spalling are minimal, and porosity is low and mostly closed. These characteristics indicate enhanced diffusion and ductility of the Ni–Cu–rich matrix, which promotes more complete homogenization and compaction compared with the 5 at.% Cu alloy.

Transitioning to the three-stage treatment (900 °C solution annealing → water quenching → 300 °C stress-relief annealing) leads to a pronounced reduction in the fraction of bright Ni_4Ti_3 precipitates and further improves the uniformity of the grain structure (Figure 9c,d). This behavior conforms to the known dissolution of Ni_4Ti_3 near 900 °C and the suppression of its re-precipitation due to rapid quenching, while subsequent low-temperature annealing relaxes internal stresses without entering the active aging range (≈350–500 °C). In SEM images, the evolution manifests as a transition from a fractured to a continuous neck network and as a decrease in both porosity and surface roughness. Based on earlier studies of Ti–Ni–Cu alloys, decreasing the density of Ni-rich precipitates and improving chemical homogeneity stabilizes the B2 austenite and promotes a single-step B2 → B19 transformation with reduced thermal hysteresis, particularly in Cu-alloyed systems.

Even after the simpler single-stage aging regime, the alloy containing 7 at.% Cu exhibits a more continuous interparticle bonding network and a more uniform microstructure than the 5 at.% Cu alloy. The three-stage heat treatment enhances these effects further by reducing secondary phases, smoothing the surface morphology, and lowering residual porosity.

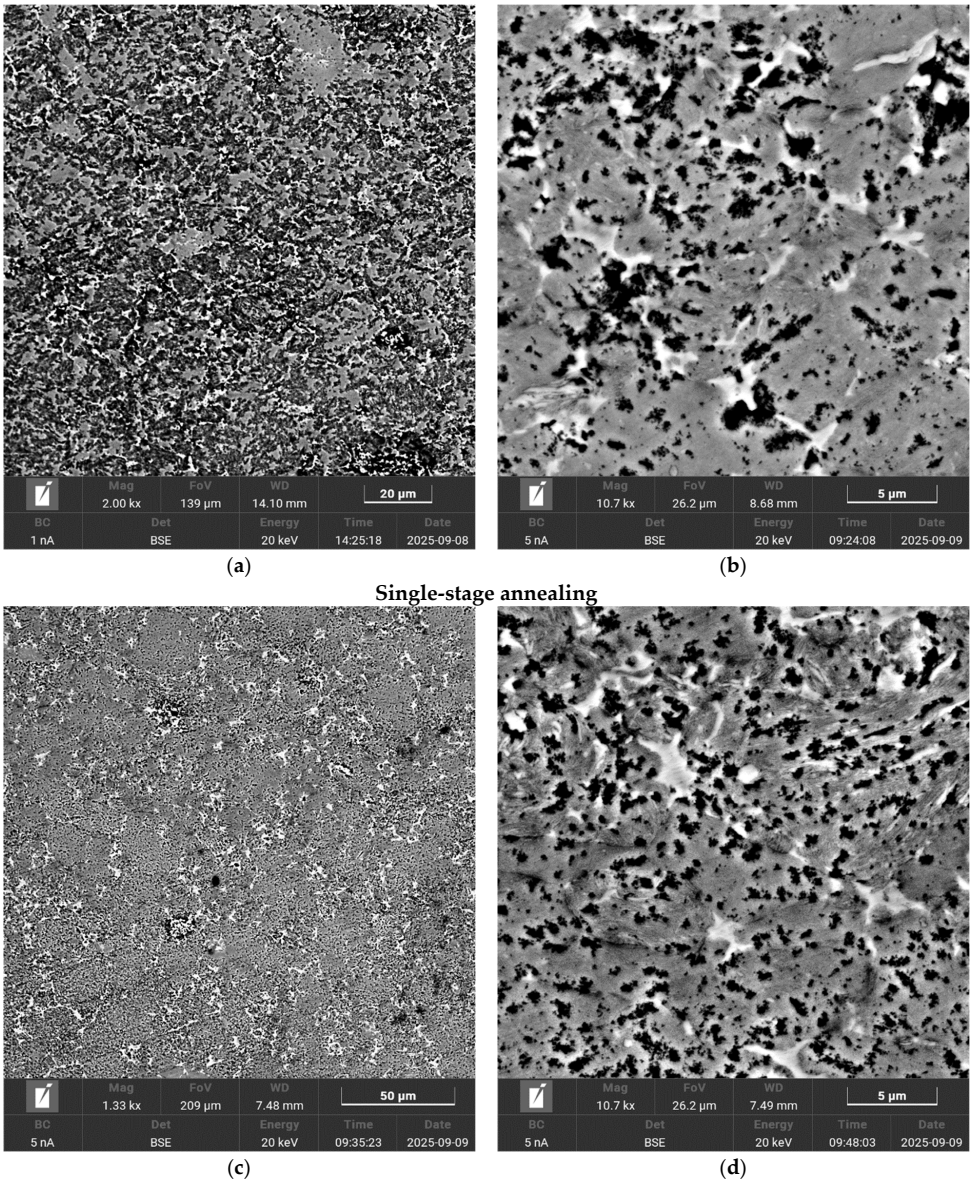


Figure 8. Surface of copper content 5% samples, after annealing: (**a**) after single-stage annealing ×1000; (**b**) after single-stage annealing ×10,000; (**c**) after three-stage annealing ×1000; (**d**) after three-stage annealing ×10,000.

The X-ray diffraction patterns of the Ni–45Ti–xCu (x = 5, 7 at.%) samples after heat treatments (Figure 10) reveal a systematic shift in phase balance toward higher fractions of highly ordered B2 austenite and a suppression of Ni-rich Ni_4Ti_3 precipitates. Both higher Cu content and the use of the three-stage regime increase this effect.

After single-stage annealing (500 °C, 2 h), both compositions exhibit B2 and B19′ reflections, along with weak Ni_4Ti_3 peaks. For 7 at.% Cu, the B2 reflections are more intense and narrower (lower FWHM), whereas the B19′ and Ni_4Ti_3 contributions are diminished, indicating improved diffusion-driven homogenization and partial relaxation of internal stresses. In the 5 at.% Cu alloy, the stronger coexistence of B2 + B19′ and more noticeable Ni-rich precipitates correspond to higher residual microstrain and heterogeneity, as evidenced by peak broadening and an increased diffuse background.

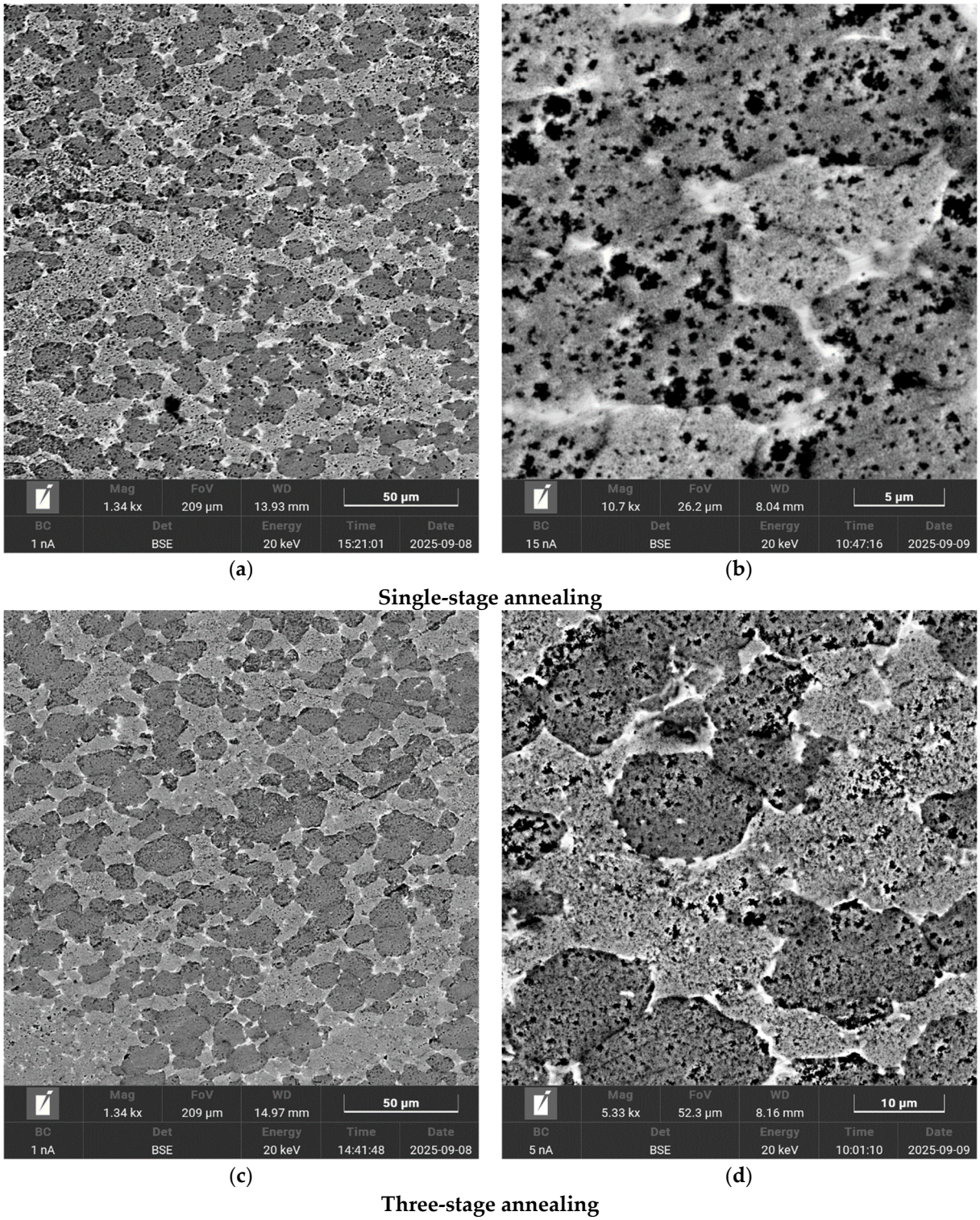
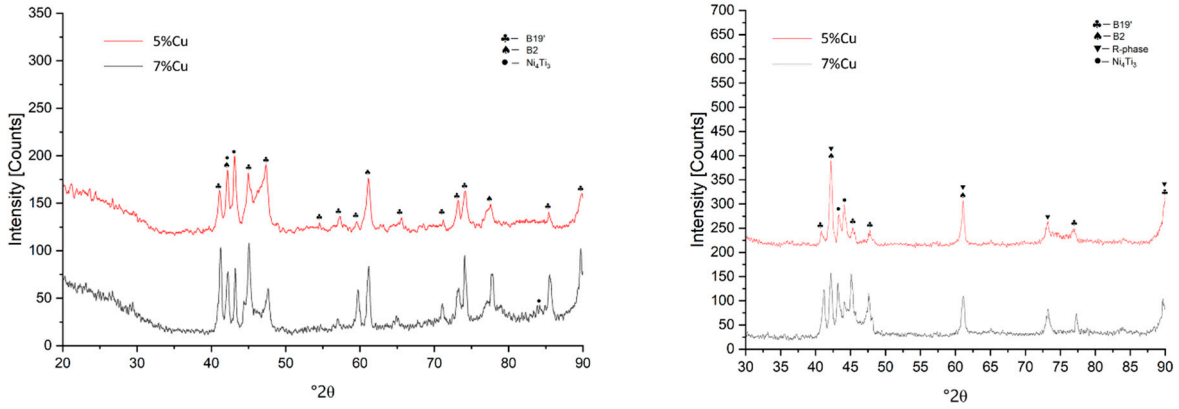


Figure 9. Surface of copper content 7% samples, after annealing: (**a**) after single-stage annealing ×1000; (**b**) after single-stage annealing ×10,000; (**c**) after three-stage annealing ×1000; (**d**) after three-stage annealing ×5000.

The high-temperature step of the three-stage treatment at 900 °C results in dissolution of Ni_4Ti_3 and matrix recrystallization: B2 peaks narrow and increase in intensity, while B19′ reflections are nearly eliminated (most clearly in the 7 at.% Cu alloy). Rapid quenching preserves the supersaturated state, preventing re-precipitation of Ni-rich phases, whereas the subsequent 300 °C annealing relieves internal stresses without activating aging reactions.

As a consequence, the alloy with 7 at.% Cu approaches a nearly single-phase B2 state. In contrast, the 5 at.% Cu alloy retains minor traces of martensite and exhibits localized reflections of the R-phase—commonly associated with lower Cu contents and incomplete stress relaxation.



(**a**) Single-stage annealing (**b**) Three-stage annealing

Figure 10. Evolution of the phase composition of samples after annealing.

Mechanistically, Cu acts via isomorphic substitution of Ni in the B2 sublattice, which reduces elastic incompatibilities at B2↔martensite interfaces and enhances interdiffusion. This shifts the transformation pathway toward a single-step B2 → B19 transition, narrows thermal hysteresis, and improves thermomechanical stability.

Overall, the combination of characteristics — increased B2 ordering, suppression of Ni_4Ti_3, and reduction of B19′/R-phase contributions — clearly shows that the Ni–45Ti–7Cu alloy subjected to the three-stage annealing achieves the most favorable phase state for enhanced functional performance. The 5 at.% Cu composition, in contrast, requires more intensive or longer diffusion treatments to fully suppress Ni-rich precipitates and residual martensite.

A semi-quantitative phase analysis was performed using the Rietveld refinement method (Table 5) in order to determine the volume fractions of the structural components in the Ni–Ti–Cu alloys after different heat-treatment regimes (Figure 10).

Table 5. Phase analysis using the Rietveld refinement method.

	Single-Stage		**Three-Stage**	
	5% Cu	**7% Cu**	**5% Cu**	**7% Cu**
B2, %	42.6	54.3	80.7	93.6
B19′, %	39.8	33.2	10.8	4.6
Ni_4Ti_3, %	17.6	12.5	1.2	0.4
R-phase, %	-	-	7.3	1.4

The obtained results show that both the Cu content and the annealing scheme have a pronounced effect on the phase composition. For the single-stage annealed samples, the 5 at.% Cu alloy contained 42.6% of the austenitic B2 phase, 39.8% of the martensitic B19′ phase, and 17.6% of the Ni_4Ti_3 phase. Increasing the Cu content to 7 at.% led to a higher fraction of the B2 phase (54.3%) and a reduction of B19′ (33.2%) and Ni_4Ti_3 (12.5%), indicating partial stabilization of the austenitic structure.

A significant transformation was observed after applying the three-stage heat-treatment scheme. In the 5 at.% Cu alloy, the B2 fraction increased to 80.7%, while the

B19′ and Ni_4Ti_3 phases decreased sharply to 10.8% and 1.2%, respectively; additionally, a small amount of R-phase (7.3%) was detected. For the 7 at.% Cu alloy, the B2 phase became dominant (93.6%), and the fractions of B19′ (4.6%), Ni_4Ti_3 (0.4%), and R-phase (1.4%) were minimal. These results clearly demonstrate that the combination of increased Cu content and multistage annealing promotes the stabilization and homogenization of the B2 austenitic matrix while suppressing secondary Ni-rich and martensitic phases.

The decisive factor in achieving high B2-phase purity and suppressing Ni_4Ti_3 precipitation is the synergistic effect of combining 7 at.% Cu with the multistage annealing regime, as confirmed by a series of comparative experiments.

X-ray diffraction analysis shows that only under the combined influence of these two factors (7 at.% Cu + three-stage annealing) does the intensity of B2 reflections increase significantly, the B19′ peaks disappear to the background level, and the Ni_4Ti_3 signals become nearly absent. In samples with lower Cu content or when only heat treatment is applied without compositional optimization, pronounced Ni_4Ti_3 peaks and a two-phase B2+B19′ state persist.

Microstructural SEM data support this conclusion: in alloys containing 7 at.% Cu subjected to multistage annealing, a continuous neck network, minimal porosity, and an almost complete absence of bright Ni_4Ti_3 inclusions are observed. In contrast, alloys with lower Cu content or after single-stage annealing exhibit coarse Ni-rich precipitates and residual martensitic regions.

Thus, the XRD and SEM results unambiguously indicate that only the combined action of optimized Cu content and the three-stage heat treatment cycle creates the conditions necessary for forming a maximally homogeneous B2 matrix. Neither an increase in Cu beyond the optimal concentration nor heat treatment alone produces a comparable effect.

4. Conclusions

This study demonstrates that a controlled combination of mechanical alloying, spark plasma sintering (SPS), and subsequent heat treatment enables targeted tailoring of the phase–structural state in Ni–45Ti–xCu alloys (x = 5 and 7 at.%). High-energy mechanical alloying results in the formation of a supersaturated FCC-(Ni, Cu, Ti) solid solution with nucleation of NiTi phases already at the powder stage. During SPS at 900 °C, a dense microstructure is developed that is dominated by the B2 austenitic phase, while the presence of B19′ martensite and Ni_4Ti_3 precipitates is minimized due to accelerated diffusion and recrystallization.

It has been established that increasing the Cu content from 5 to 7 at.% systematically enhances the stability of the B2 phase and suppresses Ni-rich secondary phases. This behavior is consistent with the isomorphic substitution of Ni by Cu in the B2 lattice and the resulting reduction in crystallographic incompatibility at transformation interfaces. The post-sintering thermal regime has a decisive influence on the final microstructure: single-stage annealing (500 °C, 2 h) retains noticeable fractions of B19′ and Ni_4Ti_3, whereas the three-stage treatment (900 °C/30 min → water quenching → 300 °C/20 min) promotes their dissolution, suppresses B19′/R transformations, and stabilizes an ordered B2 matrix. These effects are confirmed by XRD data (increased intensity and reduced FWHM of B2 reflections) as well as morphological features observed in SEM-BSE imaging—continuous interparticle neck networks, predominantly closed porosity, and the absence of bright precipitates.

The synergistic effect of increased Cu content and multistage annealing yields the most homogeneous and densified B2 matrix, significantly reducing the tendency for the formation of Ni-rich precipitates. These findings align with the established understanding that Cu promotes a shift in the transformation pathway from B2→B19′ toward B2→B19 and contributes to the narrowing of thermal hysteresis.

The key novelty of the proposed "mechanical alloying–SPS–multistage annealing" route lies in its ability to deliberately control the phase–structural state of Ni–Ti–Cu alloys, achieving a highly homogenized B2 austenitic matrix with near-complete suppression of Ni_4Ti_3. The resulting structurally uniform material exhibits a narrow thermal hysteresis loop and retains stable martensitic transformation behavior during repeated thermal cycling, which is critically important for precision actuators, sensors, and biomedical implant applications.

Author Contributions: Conceptualization, D.A., E.S., Y.K., P.K. and Y.T.; methodology, Y.K., D.A., E.S., P.K., Y.D., D.Y., A.U. and Y.T.; formal analysis, D.A., E.S., Y.K., P.K., Y.D., D.Y. and A.U.; writing—original draft preparation, Y.K., D.A., E.S., P.K. and Y.T.; supervision, Y.K. All authors have read and agreed to the published version of the manuscript.

Funding: This research was funded by the Science Committee of the Ministry of Science and Higher Education of the Republic of Kazakhstan (Grant No. AP22682739).

Data Availability Statement: The original contributions presented in this study are included in the article. Further inquiries can be directed to the corresponding author.

Conflicts of Interest: The authors declare no conflicts of interest.

References

1. Huang, W.M.; Ding, Z.; Wang, C.C.; Wei, J.; Zhao, Y.; Purnawali, H. Shape memory materials. *Mater. Today* **2010**, *13*, 54–61. [CrossRef]
2. Otsuka, K.; Ren, X. Physical metallurgy of Ti-Ni-based shape memory alloys. *Prog. Mater. Sci.* **2005**, *50*, 511–678. [CrossRef]
3. Gil, F.J.; Planell, J.A. Shape memory alloys for medical applications. *Proc. Inst. Mech. Eng. Part H J. Eng. Med.* **1998**, *212*, 473–488. [CrossRef]
4. Skakov, M.; Zhanbolatova, G.; Miniyazov, A.; Tulenbergenov, T.; Sokolov, I.; Sapatayev, Y.; Kozhakhmetov, Y.; Bukina, O. Impact of High-Power Heat Load and W Surface Carbidization on Its Structural-Phase Composition and Properties. *Fusion Sci. Technol.* **2021**, *77*, 57–66. [CrossRef]
5. Skakov, M.; Miniyazov, A.; Batyrbekov, E.; Baklanov, V.; Koyanbayev, Y.; Gradoboev, A.; Kozhakhmetov, Y.; Sokolov, I.; Tulenbergenov, T.; Zhanbolatova, G. Influence of the Carbidized Tungsten Surface on the Processes of Interaction with Helium Plasma. *Materials* **2022**, *15*, 7821. [CrossRef]
6. Bil, C.; Massey, K.; Abdullah, E.J. Wing morphing control with shape memory alloy actuators. *J. Intell. Mater. Syst. Struct.* **2013**, *24*, 879–898. [CrossRef]
7. Hartl, D.J.; Lagoudas, D.C. Aerospace applications of shape memory alloys. *Proc. Inst. Mech. Eng. Part G J. Aerosp. Eng.* **2007**, *221*, 535–552. [CrossRef]
8. Stoeckel, D. Shape memory actuators for automotive applications. *Mater. Des.* **1990**, *11*, 302–307. [CrossRef]
9. Butera, F.; Coda, A.; Vergani, G. Shape memory actuators for automotive applications. *Nanotec. IT Newsl.* **2007**, *8*, 12–16.
10. Kheirikhah, M.M.; Rabiee, S.; Edalat, M.E. A review of shape memory alloy actuators in robotics. In Proceedings of the RoboCup International Symposium, Singapore, 25 June 2010; pp. 206–217.
11. Stephen, D.; Sreekumar, M.; Nagarajan, T.; Singaperumal, M.; Zoppi, M.; Molfino, R. Critical review of current trends in shape memory alloy actuators for intelligent robots. *Ind. Robot* **2007**, *34*, 285–294.
12. Petrini, L.; Migliavacca, F. Biomedical applications of shape memory alloys. *J. Metall.* **2011**, *2011*, 501483. [CrossRef]
13. Manjaiah, M.; Narendranath, S.; Basavarajappa, S. Review on non-conventional machining of shape memory alloys. *Trans. Nonferrous Met. Soc. China* **2014**, *24*, 12–21. [CrossRef]
14. Wilson, J.; Weselowsky, M. Shape memory alloys for seismic response modification: A state-of-the-art review. *Earthq. Spectra* **2005**, *21*, 569–601. [CrossRef]
15. Dong, J.; Cai, C.; O'Keil, A. Overview of potential and existing applications of shape memory alloys in bridges. *J. Bridge Eng.* **2011**, *16*, 305–315. [CrossRef]
16. Eggeler, G.; Hornbogen, E.; Yawny, A.; Heckmann, A.; Wagner, M. Structural and functional fatigue of NiTi shape memory alloys. *Mater. Sci. Eng. A* **2004**, *378*, 24–33. [CrossRef]
17. Kockar, B.; Karaman, I.; Kim, J.I.; Chumlyakov, Y.I.; Sharp, J.; Yu, C.J.M. Thermomechanical cyclic response of an ultrafine-grained NiTi shape memory alloy. *Acta Mater.* **2008**, *56*, 3630. [CrossRef]
18. Chluba, C.; Ge, W.; Lima de Miranda, R.; Strobel, J.; Kienle, L.; Quandt, E.; Wuttig, M. Ultralow-fatigue shape memory alloy films. *Science* **2015**, *348*, 1004–1007. [CrossRef] [PubMed]

19. Tong, Y.; Gu, H.; James, R.D.; Qi, W.; Shuitcev, A.V.; Li, L. Novel TiNiCuNb shape memory alloys with excellent thermal cycling stability. *J. Alloys Compd.* **2019**, *782*, 343–347. [CrossRef]
20. Wang, H.; Cao, X.; Huang, B.; Zhang, S.; Gong, Y.; Gao, Z.; Meng, X.; Yi, X. Stability of thermal cycling and high temperature mechanical properties for Ti–V–Al–B lightweight shape memory alloy. *Prog. Nat. Sci. Mater. Int.* **2022**, *32*, 340–344. [CrossRef]
21. Lee, H.-C.; Chen, Y.-J.; Chen, C.-H. Effect of solution treatment on the shape memory functions of $(TiZrHf)_{50}Ni_{25}Co_{10}Cu_{15}$ high entropy shape memory alloy. *Entropy* **2019**, *21*, 1027. [CrossRef]
22. Firstov, G.S.; Kosorukova, T.A.; Koval, Y.N.; Verhovlyuk, P.A. Directions for high-temperature shape memory alloys' improvement: Straight way to high-entropy materials? *Shape Mem. Superelast.* **2015**, *1*, 400–407. [CrossRef]
23. Samal, S.; Molnárová, O.; Průša, F.; Kopeček, J.; Heller, L.; Šittner, P.; Škodová, M.; Abate, L.; Blanco, I. Net-shape NiTi shape memory alloy by spark plasma sintering method. *Appl. Sci.* **2021**, *11*, 1802. [CrossRef]
24. Razumov, N.G.; Makhmutov, T.Y.; Kim, A.; Goncharov, I.S.; Ozerskoi, N.E.; Silin, A.O.; Mazeeva, A.K.; Popovich, A.A. Structure and properties of a high entropy TiZrHfNiCoCu alloy obtained by mechanical alloying and spark plasma sintering. *Metallogr. Microstruct. Anal.* **2021**, *10*, 474–484. [CrossRef]
25. Kozhakhmetov, Y.; Skakov, M.; Mukhamedova, N.; Ramankulov, S.; Wieleba, W. Changes in the microstructural state of Ti-Al-Nb-based alloys depending on the temperature cycle during spark plasma sintering. *Mater. Test.* **2021**, *63*, 119–123. [CrossRef]
26. Kozhakhmetov, Y.A.; Skakov, M.K.; Kurbanbekov, S.R.; Mukhamedov, N.M.; Mukhamedov, N.Y. Powder composition structurization of the Ti-25Al-25Nb (at.%) system upon mechanical activation and subsequent spark plasma sintering. *Eurasian Chem. Technol. J.* **2021**, *23*, 37–44. [CrossRef]
27. Kozhakhmetov, Y.; Skakov, M.; Wieleba, W.; Kurbanbekov, S.; Mukhamedova, N. Evolution of intermetallic compounds in Ti-Al-Nb system by the action of mechanoactivation and spark plasma sintering. *AIMS Mater. Sci.* **2020**, *7*, 182–191. [CrossRef]
28. Shichalin, O.O.; Sakhnevich, V.N.; Buravlev, I.Y.; Lembikov, A.O.; Buravleva, A.A.; Azon, S.A.; Yarusova, S.B.; Danilova, S.N.; Fedorets, A.N.; Belov, A.A.; et al. Synthesis of Ti-Cu Multiphase Alloy by Spark Plasma Sintering: Mechanical and Corrosion Properties. *Metals* **2022**, *12*, 1089. [CrossRef]
29. Hsu, Y.-T.; Wu, C.-T.; Chen, C.-H. Nanoscale-Precipitate-Strengthened (Ni, Cu)-Rich TiNiCu Shape Memory Alloy with Stable Superelasticity and Elastocaloric Performance. *J. Alloys Compd.* **2024**, *997*, 174937. [CrossRef]
30. Kim, Y.; Choi, E. Effect of Cu addition on the martensitic transformation of powder metallurgy processed Ti–Ni alloys. *Mater. Res. Bull.* **2014**, *49*, 340–344. [CrossRef]
31. Velmurugan, C.; Senthilkumar, V.; Kesavan, J.; Ramya, K. Effects of sintering temperature on grain growth of NiTiCu shape memory alloy. *Mater. Today Proc.* **2020**, *5*, 704. [CrossRef]
32. Koch, C.C.; Whittenberger, J.D. Mechanical milling/alloying of intermetallics. *Intermetallics* **1996**, *4*, 339–355. [CrossRef]
33. Suryanarayana, C.; Klassen, T.; Ivanov, E. Synthesis of nanocomposites and amorphous alloys by mechanical alloying. *J. Mater. Sci.* **2011**, *46*, 6301–6315. [CrossRef]
34. Amini, R.; Alijani, F.; Ghaffari, M.; Alizadeh, M.; Okyay, A.K. Formation of B19′, B2, and amorphous phases during mechanosynthesis of nanocrystalline NiTi intermetallics. *Powder Technol.* **2014**, *253*, 797–802. [CrossRef]
35. Rezgoun, S.; Sakher, E.; Chouf, S.; Bououdina, M.; Benchiheub, M.; Bellucci, S. Structural, microstructural, and magnetic property dependence of nanostructured Ti50Ni43Cu7 powder prepared by high-energy mechanical alloying. *J. Supercond. Nov. Magn.* **2020**, *33*, 2059–2071. [CrossRef]
36. Sakher, E.; Loudjani, N.; Benchiheub, M.; Bououdina, M. Influence of milling time on structural and microstructural parameters of $Ni_{50}Ti_{50}$ prepared by mechanical alloying using Rietveld analysis. *J. Nanomater.* **2018**, *2018*, 2560641. [CrossRef]
37. Kim, Y.-W.; Choi, K.-C.; Chung, Y.-S.; Choi, E.; Nam, T.-H. Microstructure and martensitic transformation characteristics of gas-atomized Ti–Ni–Cu powders. *J. Alloys Compd.* **2013**, *577*, S227–S231. [CrossRef]
38. Ghadimi, M.; Shokuhfar, A.; Zolriasatein, A.; Rostami, H.R. Morphological and structural evaluation of nanocrystalline NiTiCu shape memory alloy prepared via mechanical alloying and annealing. *Mater. Lett.* **2013**, *90*, 30–33. [CrossRef]
39. Akbarpour, M.R. Effects of mechanical milling time on densification, microstructural characteristics and hardness of Cu–SiC nanocomposites prepared by conventional sintering process. *Mater. Chem. Phys.* **2021**, *261*, 124205. [CrossRef]
40. Goryczka, T.; Dercz, G. Effect of Milling Time on Crystallization Sequence and Microstructure of NiTi Alloys Produced via High-Energy Ball Milling. *Arch. Metall. Mater.* **2023**, *68*, 1127–1135. [CrossRef]

Disclaimer/Publisher's Note: The statements, opinions and data contained in all publications are solely those of the individual author(s) and contributor(s) and not of MDPI and/or the editor(s). MDPI and/or the editor(s) disclaim responsibility for any injury to people or property resulting from any ideas, methods, instructions or products referred to in the content.